Lasers in Surgery and Medicine 50:948–960 (2018)

# Optical Signature of Nerve Tissue—Exploratory Ex Vivo Study Comparing Optical, Histological, and Molecular Characteristics of Different Adipose and Nerve Tissues

**Andrea J.R. Balthasar, MD,[1*] Torre M. Bydlon, PhD,[2] Hans Ippel, PhD,[3] Marjolein van der Voort, PhD,[4] Benno H.W. Hendriks, PhD,[2,5] Gerald W. Lucassen, PhD,[4] Geert-Jan van Geffen, MD, PhD,[6] Maarten van Kleef, MD, PhD,[1] Paul van Dijk, BSc,[7] and Arno Lataster, MSc[7]**

[1]*Department of Anesthesiology and Pain Medicine, Maastricht University Medical Center, Maastricht, The Netherlands*
[2]*Philips Research, Eindhoven, The Netherlands*
[3]*Department of Biochemistry, Faculty of Health Medicine and Life Science, Maastricht University, Maastricht, The Netherlands*
[4]*Philips Healthcare, Best, The Netherlands*
[5]*Delft University of Technology, Department of BioMechanical Engineering, Delft, The Netherlands*
[6]*Department of Anesthesiology, University Medical Center St. Radboud, Nijmegen, The Netherlands*
[7]*Department of Anatomy and Embryology, Faculty of Health, Medicine and Life Sciences, Maastricht University, Maastricht, The Netherlands*

**Background:** During several anesthesiological procedures, needles are inserted through the skin of a patient to target nerves. In most cases, the needle traverses several tissues—skin, subcutaneous adipose tissue, muscles, nerves, and blood vessels—to reach the target nerve. A clear identification of the target nerve can improve the success of the nerve block and reduce the rate of complications. This may be accomplished with diffuse reflectance spectroscopy (DRS) which can provide a quantitative measure of the tissue composition. The goal of the current study was to further explore the morphological, biological, chemical, and optical characteristics of the tissues encountered during needle insertion to improve future DRS classification algorithms.

**Methods:** To compare characteristics of nerve tissue (sciatic nerve) and adipose tissues, the following techniques were used: histology, DRS, absorption spectrophotometry, high-resolution magic-angle spinning nuclear magnetic resonance (HR-MAS NMR) spectroscopy, and solution 2D $^{13}C$-$^{1}H$ heteronuclear single-quantum coherence spectroscopy. Tissues from five human freshly frozen cadavers were examined.

**Results:** Histology clearly highlights a higher density of cellular nuclei, collagen, and cytoplasm in fascicular nerve tissue (IFAS). IFAS showed lower absorption of light around 1200 nm and 1750 nm, higher absorption around 1500 nm and 2000 nm, and a shift in the peak observed around 1000 nm. DRS measurements showed a higher



Conflict of Interest Disclosures: All authors have completed and submitted the ICMJE Form for Disclosure of Potential Conflicts of Interest and have disclosed the following: None of the authors who are affiliated with clinical institutions has financial interests in the subject matter, materials, or equipment or with any competing materials. The Maastricht University Medical Center received research funding from Philips to carry out the work described. The author affiliated with this institution (A.J.R.B.) received no payment for participation in this research project. G-J.v.G served as consultant to Philips and received compensation for these services. The terms of the consultancy have been reviewed and approved by the Radboud University Medical Center in accordance with its policy on objectivity in research. His institution did not receive payment for anything beyond the direct costs of performing the research project. All of the authors who are affiliated with Philips Research and Philips Healthcare have financial interests in the subject matter, materials, and equipment, in the sense that they are employees of Philips. The prototype system described in this article is currently a research prototype and is not for commercial use.

Departments/institutions to which the work is attributed: Department of Anesthesiology and Pain Medicine, Maastricht University Medical Center, Maastricht, The Netherlands and Department of Anatomy and Embryology and Department of Biochemistry, Maastricht University, Maastricht, The Netherlands and Philips Research, Eindhoven, The Netherlands.

Trial Registration: Not applicable.

Contract grant sponsor: Philips Research, Eindhoven, The Netherlands.

*Correspondence to: Andrea J.R. Balthasar, MD, Maastricht University Medical Center, Department of Anesthesiology and Pain Medicine, P.O. Box 5800, 6202 AZ Maastricht, The Netherlands. E-mail: a.balthasar@gmx.de

Accepted 20 April 2018
Published online 14 May 2018 in Wiley Online Library (wileyonlinelibrary.com).
DOI 10.1002/lsm.22938

water percentage and collagen concentration in IFAS and a lower fat percentage compared to all other tissues. The scattering parameter (b) was highest in IFAS. The HR-MAS NMR data showed three extra chemical peak shifts in IFAS tissue.

**Conclusion:** Collagen, water, and cellular nuclei concentration are clearly different between nerve fascicular tissue and other adipose tissue and explain some of the differences observed in the optical absorption, DRS, and HR-NMR spectra of these tissues. Some differences observed between fascicular nerve tissue and adipose tissues cannot yet be explained but may be helpful in improving the discriminatory capabilities of DRS in anesthesiology procedures. Lasers Surg. Med. 50:948–960, 2018. 

**Key words:** nerve fascicle; adipose tissue; HR-MAS NMR; optical; absorption; diffuse reflectance spectroscopy; histology

## OBJECTIVES

In surgical and anesthesiological practice, the identification of different tissue types is essential. During several (regional) anesthesia and pain medicine procedures, needles are inserted through the skin of a patient to target nerves. Nerves are targeted to anesthetize an operation area and to treat acute postoperative pain [1]. In most cases, the needle traverses several tissues—skin, subcutaneous adipose tissue, muscles, nerves, and blood vessels—to reach the target nerve. A clear identification of the target nerve can improve success of the nerve block and reduce the rate of complications [2]. Current localization techniques, which include ultrasound or X-ray guidance, angiography, aspiration, and nerve stimulation, help the clinician to guide the needle to the target but are not without their limitations [2–7]. Ultrasound with or without nerve stimulation is at the moment the most appropriate technique used during locoregional anesthesia. The identification of nerves with ultrasound is highly dependent on the anatomical knowledge, the skills and interpretation of the information by the operator, and the echogenic characteristics of the patient and the nerves [8,9]. In locoregional anesthesia, nerve stimulation is only capable of identifying the nerve in 74.5% of the cases [10]. Despite the use of ultrasound, nerve stimulation, and other precautions during injection, cases of nerve damage are still reported [11–13]. The incidence of complications after locoregional anesthesia is 4–6 per 10,000 blocks [14–17]. Patients and clinicians fear neurological complications, such as leg weakness or neuropathic pain [18,19]. Even temporary nerve damage has a major impact on the quality of life of the patient [20]. Most neurological damage recovers in a year. However, more serious complications are reported after interventional pain therapy at the spinal level. Reports of spinal cord damage, brain infarctions, and death have been published [19,21–26].

The majority of the complications are due to direct or indirect damage of the nerves and unintended injection of local anesthetics into blood vessels [18,27]. Damage to more distal parts of a nerve tend to occur less often and are less severe than damage to more proximal parts [28–30]. One explanation could be that the tissue composition of peripheral nerves changes proximally to distally. The nerve root at the foraminal level of the spine is more solid and consists mostly of one large fascicle [31,32]. Along their course, the fascicle branches and more connective and adipose tissue and blood vessels surround the fascicles in the nerve structure [28,29]. The most vulnerable structures to needle damage are the nerve fascicles and the supplying microvessels [16,33].

A clear identification of the tissue in front of the needle tip may further improve the performance and safety of needle-based interventions. One such technique that can provide a quantitative measure of the tissue composition (lipid, water, blood content, etc.) at the tip of a needle is diffuse reflectance spectroscopy (DRS) [34,35]. The feasibility of DRS for a variety of clinical applications has already been reported [36–41]. The basic principle involves delivering light into tissue with a small optical fiber and collecting reflected light with another optical fiber after it has undergone absorption and scattering events within the tissue. Depending on the presence and concentrations of light-absorbing molecules in the tissue, the light is absorbed differently, thus creating a specific fingerprint of the tissue. Prominent absorbers in biological tissue are hemoglobin, water, collagen, and lipids [34,35,42,43]. Tissues that contain different amounts of these absorbers can be discriminated from each other [44]. In an earlier *in vivo* study on optical detection of peripheral nerves, we concluded that differentiation between nerves in a fatty surrounding was difficult [40,41,45]. In a more recent study in human cadavers, we found a sensitivity and specificity of 90% for discrimination of whole nerve tissue from surrounding tissues [32]. In an *in vivo* study using DRS during surgery, peripheral nerves were detected with an sensitivity of 85% and a specificity of 79% [46]. In another study, nerve tissue was compared between human and swine, *in vivo* and *ex vivo*, in order to develop alternative validation models for optical technologies; with wavelengths of 400–1600 nm, a strong positive correlation was found between the models [47]. In all these studies, the nerve was considered as one entity, and we did not account for the various structures that make up the nerve bundle. Furthermore we used light in the range of 400–1600 nm.

We recognize though that the nerve is a very heterogeneous tissue and in order to detect when the tip of a DRS needle is inside the nerve, the optical properties of different nerve components have to be known. This is necessary to prevent injection of the anesthetic inside the fascicular nerve tissue. Therefore, one goal of the current work was to investigate the optical characteristics of fascicular and non-fascicular nerve tissues. In addition, to better understand the strengths and limitations of DRS in the context of anesthesiology procedures and in particular for the prevention of intrafascicular needle placement, it was our objective as well to improve knowledge of the tissue composition of tissues surrounding the nerve and along the

needle trajectory. For instance, when differences are observed in the optical characteristics of the relevant tissues, and these can be linked with morphological, biological and/or chemical characteristics, discriminatory algorithms for DRS in regional anesthesia procedures could be improved.

The above-described objectives were formulated in the form of the following research questions:

1. What are the histological differences between subcutaneous fat (SCF), fat close to the sciatic nerve (adnexa/sliding fat, ADF), sciatic non-fascicular nerve tissue (NFAS), and sciatic fascicular nerve (IFAS) tissue?
2. What are the optical differences between the four tissues? Can we explain these differences by the histological findings?
3. Besides a histological explanation is there also a molecular explanation (HR-NMR) of the differences?

## METHODS

The study was performed in collaboration with the Department of Anatomy and Embryology and the Department of Biochemistry of the Faculty of Health Medicine and Life Science (Maastricht University, Maastricht), the Department of Anesthesiology and Pain Medicine (University Hospital of Maastricht), and Philips Research (Eindhoven), all located in the Netherlands. A handwritten and signed codicil from each donor, as required by Dutch law for scientific research and education, is kept at the Department of Anatomy and Embryology.

To compare characteristics of human nerve tissue and adipose tissues, the following techniques were used: histology, DRS, absorption spectrophotometry, high-resolution magic-angle spinning nuclear magnetic resonance (HR-MAS NMR) spectroscopy, and solution 2D $^{13}C$-$^{1}H$ heteronuclear single-quantum coherence (HSQC) spectroscopy. The reasoning for using these methods was as follows: our group has incorporated DRS into anesthesiology needles to differentiate tissues. Differences in the optical properties of the tissues form the basis of the discriminating abilities of DRS. These optical properties, namely absorption and scattering coefficients, must be derived from the DRS spectra. This can be done with various techniques (we use an analytical model developed by Farrell et al. [48]) but requires a number of assumptions to be made, especially about the absorbers that are present in the tissue. Therefore, if there are unknown absorbers in the tissue, the results obtained from the DRS measurements may be less accurate.

A spectrophotometer can be used to determine the absorption and scattering coefficients of the tissue directly without making assumptions regarding the fiber measurement geometry or the absorbers in the tissue. Additionally, a larger wavelength range can be explored which may show other differences between tissue types that typical DRS systems are not capable of sensing.

Histology was employed in this study to examine the tissues on a microscopic level. By using various staining techniques, the presence of certain cellular structures was investigated to explore if differences observed between the tissue types could be explained by morphological/cellular differences.

HR-MAS NMR and HSQC spectroscopy methods can be used to determine physical and chemical properties of organic molecules (such as proteins and nucleic acids). The methods were employed in this study to explore if differences between the tissue types could be related to certain molecular/chemical differences.

Details of the different methods are described below.

### Sample Size and Statistical Analysis

To our knowledge, no comparable studies have been reported. Due to the exploratory nature of the study, no input data for a power analysis were available. The study is a qualitative study aiming at investigating trends in the data. We therefore decided to only use descriptive statistics and indicate where possible confidence intervals and standard deviations.

### Anatomy-Histology

**Anatomy.** Tissues from five human freshly frozen cadavers were examined. None of the individuals died

**TABLE 1. Overview of the Cadavers Included With Patient Characteristics and the Measurements Performed**

| | | | | HNMR,Measurements | |
|---|---|---|---|---|---|
| Cadaver #/ sex/age in years | Date tissue extracted | DRS measurements | Absorption measurements | HR-MAS NMR/ | 2D $^{13}C$-$^{1}H$ HSQC |
| 1/Female/76 | November 2014 | — | SCF, ADF, NFAS, IFAS | — | — |
| 2/Male/78 | November 2014 | SCF, ADF, NFAS, IFAS | SCF, ADF, NFAS, IFAS | SCF, ADF, NFAS, IFAS | — |
| 3/Male/86 | November 2014 | SCF, ADF, NFAS, IFAS | SCF, ADF, NFAS, IFAS | SCF, ADF, NFAS, IFAS | SCF, ADF, NFAS, IFAS |
| 4/Female/91 | August 2015 | SCF, NFAS, IFAS | — | — | IFAS |
| 5/Female/86 | August 2015 | SCF, NFAS, IFAS | — | — | — |

SCF, subcutaneous fat; adnexa/sliding fat, ADF, fat close to sciatic nerve; IFAS, sciatic fascicular nerve tissue; NFAS, sciatic non-fascicular nerve tissue.

due to a neurological disease. Table 1 provides an overview of the cadavers and the measurements performed on each sample. Certain measurement techniques were not available for all tissue samples.

As a target region, the sciatic nerve was chosen because of its size. In the upper leg, samples of subcutaneous fat (SCF), fat close to the sciatic nerve (adnexa / sliding fat, ADF), sciatic fascicular nerve (IFAS) tissue, and sciatic non-fascicular nerve (NFAS) tissue were dissected. Adipose tissue is composed of collagen and adipocytes filled with fat droplets; adipose tissue is referred to as fat in the text below [47]. Figure 1 shows an anatomical drawing of the sciatic nerve, including descriptions of the different structures that make up the nerve bundle. The figure also shows a bifurcated sciatic nerve and the fascicles microscopically dissected from the nerve bundle.

Fat samples were collected macroscopically. Three SCF and ADF samples with a volume of 2 ml per cadaver and a piece for cross-sectional histology were saved. For the collection of 2 ml of fascicular and non-fascicular nerve tissue, a microscope was used. Immediately after preparation of the samples, samples were frozen (liquid nitrogen, $-196^{\circ}$C and stored at $-20^{\circ}$C) or fixed (4% neutral-buffered formaldehyde for 24 hours).

**Histology.** Two different staining techniques were used to differentiate between the different tissue compositions: Mayer's hematoxylin and eosin stain (H&E stain) to color cell nuclei blue and cytoplasm pink; [49] osmium tetroxide ($OsO_4$) to color lipids black [50]. Parts of the samples containing fat were post-fixed in 1% $OsO_4$ in phosphate-buffered saline (PBS), pH 7.4; the other samples were fixed in 4% neutral-buffered formaldehyde. After de-paraffinization, they were stained according to the selected staining protocol [51].

The fixed and post-fixed tissues were embedded separately in paraffin. Then, 4-μm-thick histological sections of the sciatic nerve and IFAS tissue and 7-μm-thick sections of the other tissues were cut on a Leica 2245 microtome. The sciatic nerve and IFAS tissues were cut transversely; the ADF, SCF, and NFAS tissues were cut in a direction suitable to obtain a large tissue area.

## Optical Data Collection

**Absorption spectrophotometry.** The tissues were removed from the freezer and brought to room temperature. For each type of tissue, a 1-mm cuvette was filled, while keeping the tissue homogenous throughout the length of the cuvette.

A Perkin Elmer spectrophotometer with a single integrating sphere was used to measure the total transmittance, collimated transmittance, and diffuse reflectance of each sample (300–2300 nm). The spectrophotometer was 0% and 100% background-corrected before any measurements. A stray light measurement was also taken to correct the diffuse reflectance spectra; this accounts for any light that might be scattered within the integrating sphere prior to reaching the sample itself. The measured reflectance ($R_{meas}$) was corrected with known Spectralon data ($R_{100}$) and the stray light ($R_0$) measurement. Diffuse reflectance was therefore defined as:

$$R_d = \frac{R_{100}(R_{meas} - R_0)}{100 - R_0}$$

Collimated transmittance ($T_c$) and total transmittance ($T_t$) measurements were used to calculate the diffuse

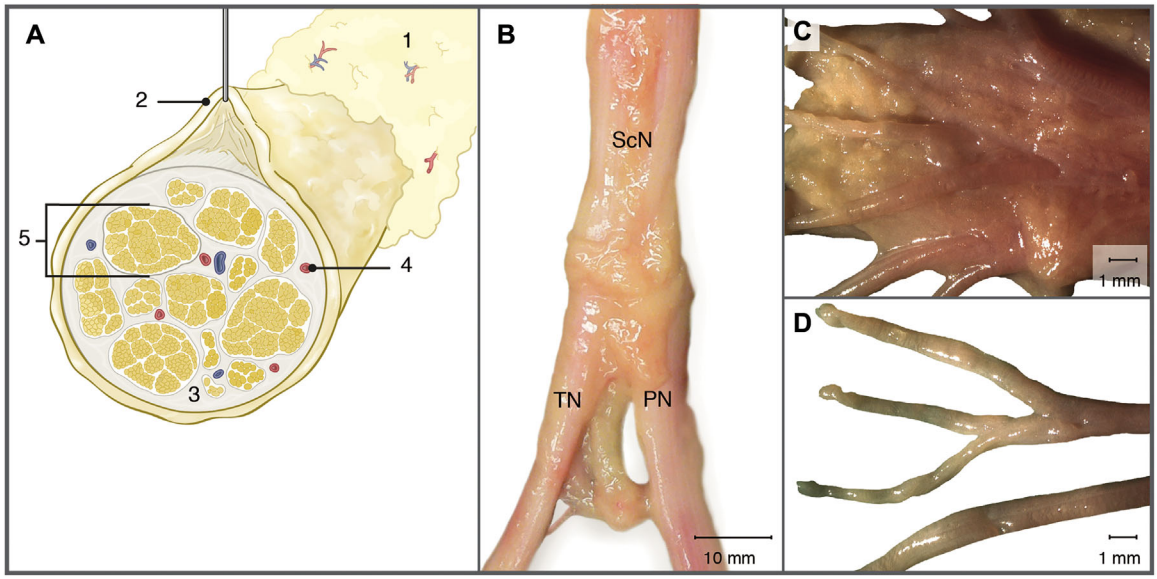


Fig. 1. (**A**) Anatomical drawing of a cross-section of a nerve: (1) subcutaneous adipose tissue, (2) adnex adipose tissue (sliding fat), (3) non-fascicular nerve tissue and epineurium, (4) blood vessel, and (5) fascicular nerve tissue and perineurium. (**B**) Part of a sciatic nerve with bifurcation to the tibial (TN) and peroneal (PN) nerve. (**C**)Fascicles of a sciatic nerve with surrounding epineurium D: Fascicles without epineurium.

transmittance ($T_d$):

$$T_d = T_t - T_c$$

The Kubelka-Munk equations were then used to calculate the absorption coefficient in units of $cm^{-1}$ [52].

### Diffuse Reflectance Spectroscopy Measurements

Frozen tissue samples were brought to room temperature and placed in glass cylinders. Ten diffuse reflectance spectra (400–1600 nm) were acquired from the tissue samples at ~5 different locations with a custom-designed optical needle and an optical console [53]. The optical needle had a 0.837-mm distance between the two 200-μm illumination and collection fibers and was used to relay light to and from the tissue to the optical console. The optical console consisted of a broadband light source and two spectrometers: one to record data in the visible wavelength range and the other for the near-infrared wavelengths. The spectra were corrected for daily variations in optical throughput using a Spectralon calibration standard. Several models have been described in the literature to express the intensity of light collected by a fiber after several scattering and absorption events in a diffuse medium [54–58]. The model that is used in this paper is explained in earlier publications and corresponds to the solution of the diffusion equation for a semi-infinite medium and is a widely accepted model in the field of biomedical photonics [48,53,59,60]. The fitting algorithm in the model utilizes the absorption coefficients of known tissue absorbers to determine the volume fraction of each absorbing element in the measured tissue, while taking into account tissue-scattering characteristics as well. For the analysis of the data collected for this study, the following absorbers were included in the fit model: oxygenated and deoxygenated hemoglobin, methemoglobin, water, fat (using the measured absorption coefficient of SCF), β-carotene, and collagen. We note that the collagen absorption spectra were obtained on a relative scale. Therefore, collagen concentrations will be provided with arbitrary units. Scattering-related parameters included were: Mie scattering (fmie), the Mie slope parameter (b), and the scattering at 800 nm (S800) [32].

### HR-MAS and 2D $^{13}$C-$^{1}$H HSQC NMR Data Acquisition and Processing

$^{1}$H HR-MAS NMR (high-resolution magic-angle spinning nuclear magnetic resonance) spectra were acquired at 295 K on a Bruker Avance I narrow bore, 600 MHz NMR spectrometer, equipped with a 14.1 Tesla superconducting magnet and a 4 mm $^{1}$H/$^{13}$C HR-MAS probe at a spinning rate of 6000 Hz. The spectra were obtained under unlocked conditions. High-resolution NMR spectra of tissue extracts in deuterated chloroform ($CDCl_3$) and dimethyl sulfoxide (DMSO-$d^6$) were recorded at 298 K on a Bruker Ascend HD 700 MHz NMR spectrometer, equipped with a cryogenically cooled Triple Resonance Probe (TCI) probe. Typically, 32–128 scans were collected for a 1D proton spectrum using an inter-scan relaxation delay of 5 seconds.

At a later stage, a more detailed molecular analysis was done by acquiring a natural-abundance 2D $^{13}$C-$^{1}$H HSQC spectrum of selected IFAS tissue extracts, in order to classify constitutive lipid components. Typically, 2 to 4 scans and 512 increments over a spectral width of $^{13}$C 160 ppm were collected.

## RESULTS

### Anatomy and Histology

The H&E-stained SCF and ADF slides showed large accumulations of fat cells separated by elongated and elaborated collagenous connective tissue structures and blood vessels (Fig. 2).

The H&E-stained cross-sections of the sciatic nerve showed several nerve fascicles. An outer, loose fibrocollagenous epineurium containing fat surrounded the intact nerve. The epineurium continued between the individual fascicle groups as an inner, inter-fascicular epineurium, with fat and blood vessels. The perineurium, consisting of concentric layers of flattened cells and collagenous connective tissue, surrounding and invading smaller groups of fascicles, and the endoneurium around and between groups of axons, were less visible. The osmium tetroxide (OsO4)-post-fixed cross-sections of the sciatic nerve showed the latter, more detailed aspects better, as well as the fat in the inter-fascicular epineurium and in the myelin sheaths around the myelinated axons (Fig. 2). The cytoplasm surrounds the cell nuclei (stained blue in Fig. 2A + C). In the fat cells, the cytoplasm is filled with (fused) fat vacuoles and forms a thin layer against the inner side of the cell membrane.

### Optical Data

**Absorption coefficients.** Figure 3 shows the measured absorption coefficients averaged across three cadavers. NFAS, SCF, and ADF show many similarities, while IFAS is most notably different around 1200 nm, 1500 nm, 1750 nm, and 2000 nm. Additionally, a red shift is observed in the peak near 1000 nm, which is only seen in the IFAS tissues.

**Diffuse reflectance spectra.** Figure 4A shows the DR spectra for the various measured tissues averaged over all measurement locations and four cadavers. Overall, little difference is seen between SCF and ADF. Although NFAS has a higher intensity, the general shape is similar to the ADF and SCF spectra. IFAS has the highest intensity; with differences seen in the slope (reflective of a scattering difference), around 1000 nm, 1200 nm, and above 1400 nm.

The fit parameters extracted from the spectra can be seen in Figures 4B–F. Blood and oxygen saturation (StO2) are highly variable between cadavers and do not show any trends. Collagen is higher in IFAS compared to NFAS, ADF, and SCF. The scattering parameters s800 and fmie show little trends, while scattering slope (b) does appear higher in IFAS compared to the others. Fat is lowest in IFAS, with comparable values between the other tissues, while water shows the opposite trend. No trend is seen in β-carotene.

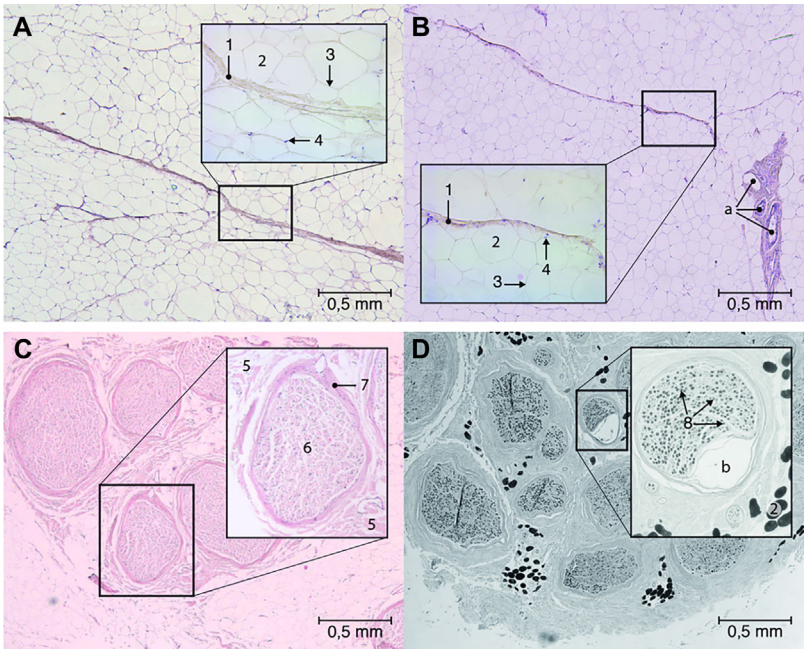


Fig. 2. Histology of (**A**) SCF stained with H&E, (**B**) ADF stained with H&E, (**C**) cross-section of sciatic nerve stained with H&E, and (**D**) cross-section of sciatic nerve stained with Osmium Tetroxide. H&E colors cell nuclei blue and cytoplasm pink, and Osmium Tetroxide colors lipids black. (1) Collagenous fibers, (2) fat vacuole(s), (3) cytoplasm, (4) nucleus, (5) epineurium, (6) endoneurium, (7) perineurium, (8) myelin sheet (Schwann cells consisting of nuclei, cytoplasm, proteins, and lipids), (a) blood vessels, and (b) artifact. SCF, subcutaneous adipose tissue; H&E, Mayer's hematoxylin and eosin stain; ADF, adnex adipose tissue.

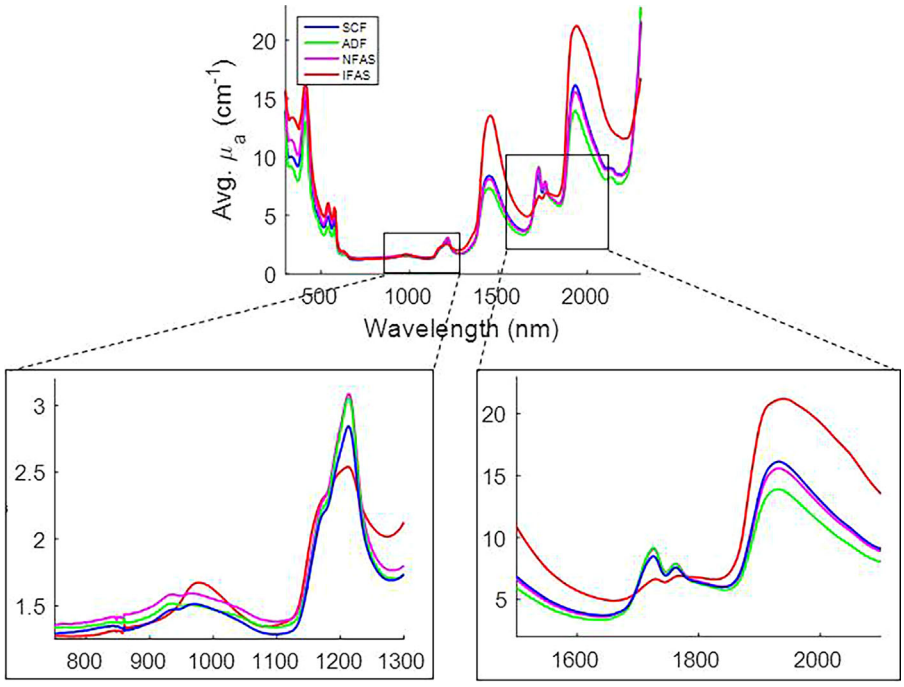


Fig. 3. Tissue absorption coefficients measured with a spectrophotometer showing the full wavelength range and two separate wavelength regions.

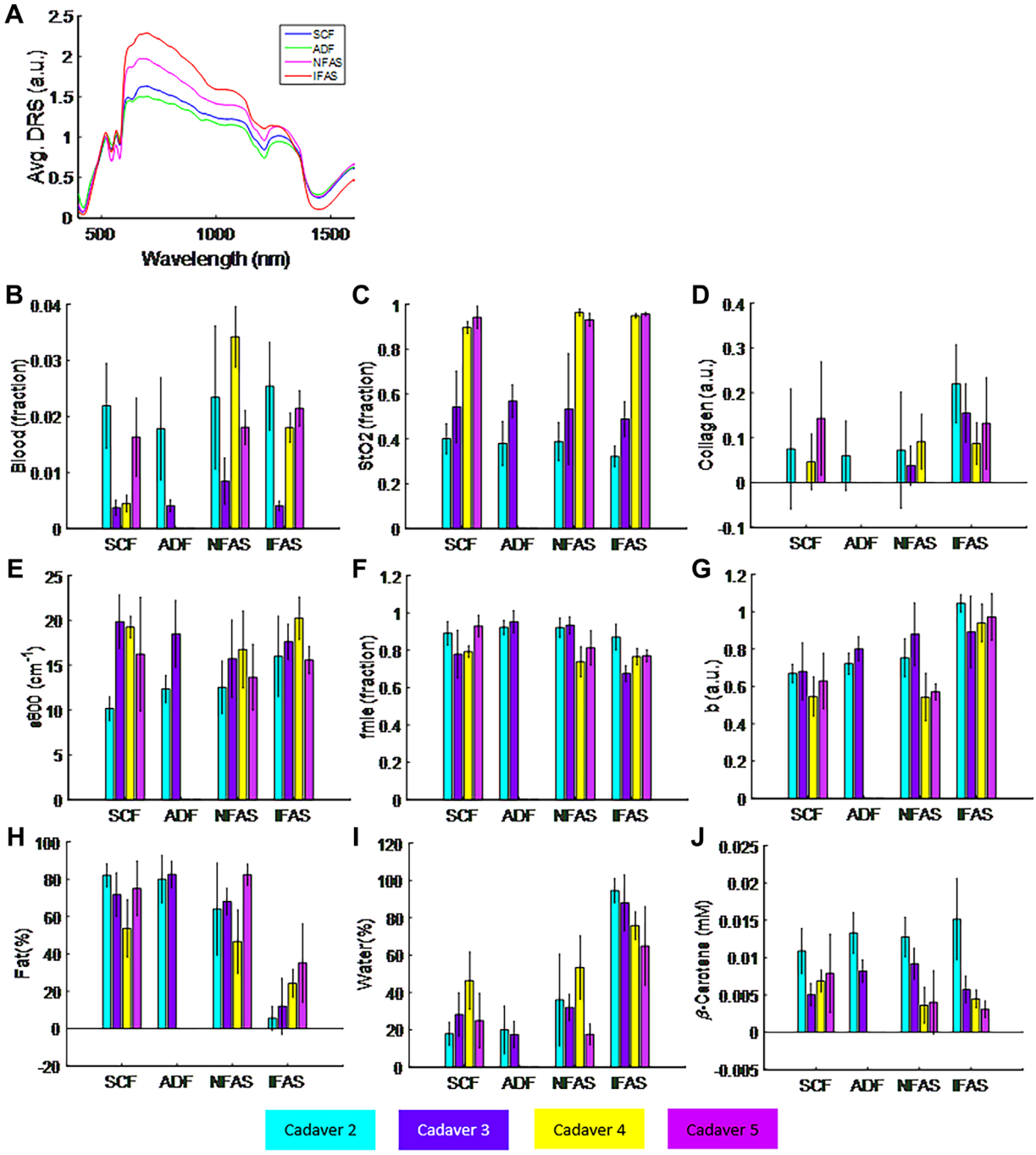


Fig. 4. (**A**) Diffuse reflectance spectra averaged over multiple sites and cadavers. (**B–J**) Bar graphs of the fit parameters extracted from the diffuse reflectance spectra plotted per cadaver and per tissue type. The bar represents the average of all sites within a cadaver and the black whisker is the 95% confidence interval. IFAS = sciatic fascicular nerve tissue. NFAS = sciatic non-fascicular nerve, SCF = subcutaneous adipose tissue, ADF = adnex adipose tissue. Units: A, D, G have arbitrary units. (**B**) Blood is total hemoglobin fraction under the assumption that full blood contains 150 Hemoglobin mg/ml since 1 = 100% Total Hemoglobin. (**C**) StO2 is tissue oxygenation fraction 1 represents 100% tissue oxygenation. (**E**) s800 is in $cm^{-1}$. (**F**) fmie is the fraction of Mie over Rayleigh scattering. (**G**) b is a dimensionless parameter so we write this as arbitrary units. (**H** and **I**) are percentages. (**J**) β-carotene is in mM.

### HR-MAS and 2D $^{13}$C-$^{1}$H HSQC NMR Spectroscopy

Samples from cadavers 2 and 3 were studied by HR-MAS and 2D $^{13}$C-$^{1}$H HSQC NMR spectroscopy. The proton HR-MAS NMR spectra of all four tissues (IFAS, NFAS, ADF, and SCF) are shown in Figure 5A and B. Eleven resolved proton signals are observed; corresponding chemical shifts and assigned chemical groups of the associated molecules are listed in Table 2. In order to compare the water content of the samples, the spectra were normalized on the intensities of the triglyceride-$CH_3$ signal. Signals of triglyceride (signals 1, 2, 4–11) and water (signal 3) can be distinguished in the spectra of all samples. These were used to extract the water and lipid content of the different tissues, for comparison with the estimates of lipid and water content, based on DR measurements (Fig. 5C and D).

The IFAS spectrum (cadaver 3) contains a few additional signals (at 3.01, 3.20, and 5.77 ppm), which indicate the presence of a component comprised of unsaturated lipid protons (5.77 ppm) and a choline head group moiety (around 3 ppm). A search was done to identify the extra peaks. 2D $^{13}$C-$^{1}$H HSQC spectra were recorded to correlate protons to their bound carbon atoms. $^{13}$C chemical shifts span a larger chemical shift range and are better indicators for the presence of certain chemical groups. Extraction of IFAS tissue material by $CDCl_3$-MeOH (2:1 v/v) and/or DMSO-d$^6$ was carried out to detect lipid constituents by means of 1D 1H and 2D $^{13}$C-$^{1}$H HSQC solution NMR at 700 MHz. These results

**TABLE 2. Assignment of the 1H-NMR Signals**

| Signal # | Assignment |
|---|---|
| 1 | CH of a lipid chain double-bond |
| 2 | CHO of glycerol head group |
| 3 | $H_2O$ |
| 4 | $CH_2O$ of glycerol head group |
| 5 | $CH_2O$ of glycerol head group |
| 6 | $CH_2$ in between two double-bonds |
| 7 | $(C=O)CH_2$ (next to ester) |
| 8 | $CH_2$ next to double-bond |
| 9 | $(C=O)CH_2CH_2$ |
| 10 | $CH_2$ |
| 11 | $CH_3$ |

This table presents a detailed overview of the assignment of the 11 identified signals (Fig. 5).

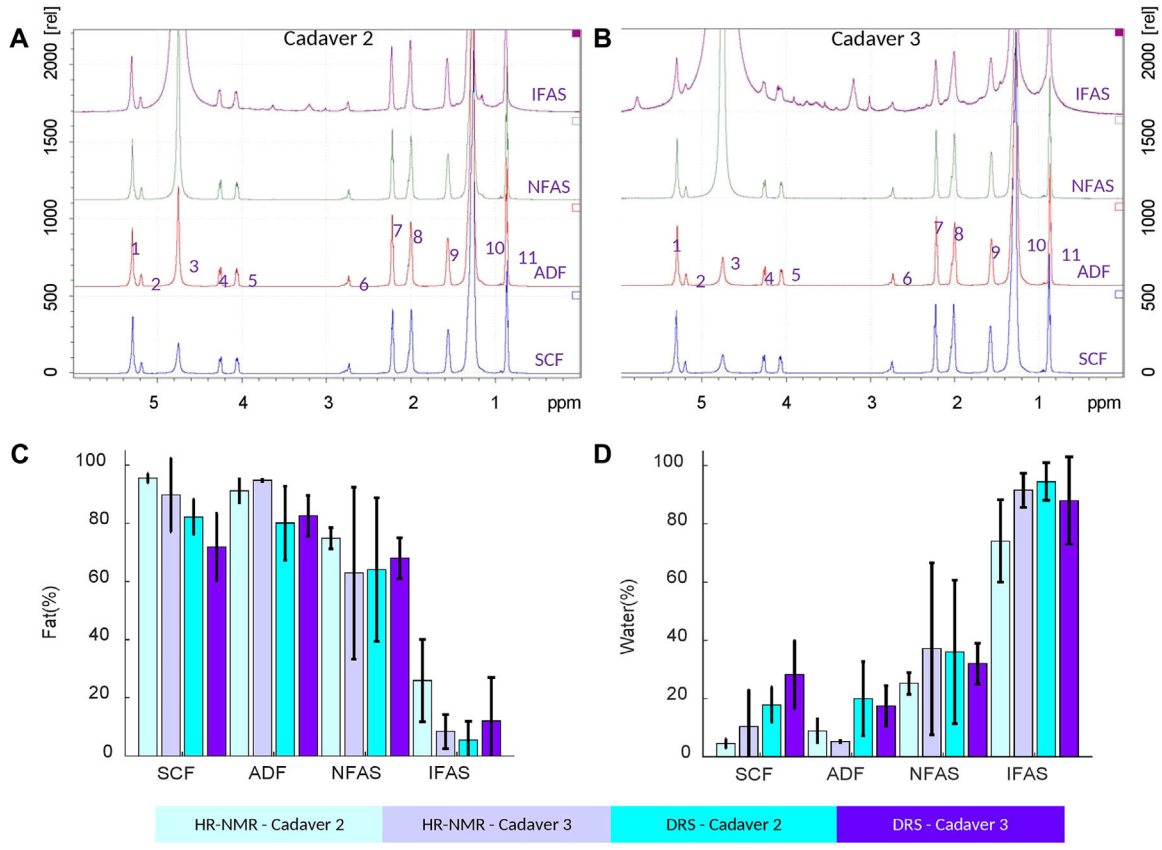


Fig. 5. Results from cadavers 2 and 3. (**A** and **B**) HR-NMR results of IFAS, NFAS, ADF, and SCF (part per million [ppm], recommended exposure limit [rel]). (**C** and **D**) Fat and water percentages extracted from the HR-NMR data and DRS. Mean and 95% confidence interval are presented. IFAS, sciatic fascicular nerve tissue; NFAS, sciatic non-fascicular nerve; SCF, subcutaneous adipose tissue; ADF, adnex adipose tissue.

confirm the triglyceride lipid composition from HR-MAS NMR but failed to detect the extra peaks of the unidentified compound (Supplements S1 and S2). DMSO extracts of pre-washed chloroform/methanol fractions of IFAS, where abundant apolar triglycerides are removed from solution, show indeed more polar lipid compounds in solution that contain resonances with chemical shifts compatible with the presence of choline groups (Supplement S1). The assignment of the main lipid signals is represented in Table 2.

## DISCUSSION

Discrimination of nerve fascicles from other surrounding tissues is essential to prevent possible complications due to percutaneous needle-based interventional procedures in anesthesiological practice. In anesthesiological literature, the ideal needle tip location during a nerve block is a point of discussion. Some opinion leaders state that it is safe to put the needle tip in NFAS as long as you do not injure IFAS [61]. On the other hand it is very difficult to judge during an ultrasound guided procedure where exactly the needle tip is. In clinical practice, despite real-time visualization of the needle tip with ultrasound, needle to nerve contact or epineurium perforation, cannot be prevented [62]. Unintentional intraneural injection occurs at an incidence rate of 16.3% for the ultrasound-guided subgluteal approach to the sciatic nerve [63]. Therefore, the concept of identifying tissue types in front of the needle during the procedure is very interesting for all kinds of percutaneous needle based procedures, especially those performed in anesthesiological practice.

Previous studies have shown that DRS can differentiate between adipose tissue, muscle, and blood [32,38–41,45]. Our previous *ex vivo* DRS study demonstrated a sensitivity and specificity of 90% in discriminating whole nerve tissue compared to surrounding tissue [32]. The aim of the current study was to investigate the basis for the difference between the DRS data of IFAS and surrounding tissues, by using histology, optical absorption measurements, DRS, and H-NMR and comparing the results. We chose the sciatic nerve because of its size and sufficient surrounding adipose tissue.

In the DRS spectra we found unique signatures in IFAS, which we further investigated trying to describe these signatures down to the molecular level. Table 3 provides an overview of the main differences between IFAS and the other tissues, as observed with the various measurement techniques. Here, we summarize the findings:

Histology clearly highlights a higher density of cellular nuclei, collagen, and cytoplasm (consisting of >80% water) in IFAS tissue (Fig. 2).

Optical absorption measurements also showed clear differences between IFAS and the other tissues: compared to the other tissues, IFAS showed lower absorption around 1200 nm and 1750 nm, higher absorption around 1500 nm and 2000 nm, and a shift in the peak observed around 1000 nm.

The estimates of chromophore concentrations and scattering parameters based on the DRS measurements showed a higher water percentage in IFAS and a lower fat percentage compared to all other tissues. Also, the collagen concentration appeared higher in IFAS compared to ADF and SCF. The scattering parameter (b) related to Mie scattering was highest in IFAS.

Finally, the HR-MAS NMR data showed three extra chemical peak shifts in IFAS tissue (3.0–3.2, 3.4, and 5.7–5.8 ppm). Estimates of the water and lipid content based on the HR-MAS NMR data indicated a high water and low lipid content in IFAS and *vice versa* for the other tissues.

When comparing the observations from the different methods, consistencies are observed:

Estimates of the water and lipid contents appear consistent for DRS and HR-NMR and are confirmed by histology. Also, the differences in optical absorption can probably be explained by this: the shape difference around 1200 nm is likely due to a lack of fatty tissue in the IFAS sample.

The collagen content estimated from DRS is highest in IFAS, which is confirmed by histology, as well. Then, looking again at the optical absorption, the lower absorption in IFAS >1400 nm is likely caused by increased absorption by water and collagen.

Scattering is related to refractive index changes present in the tissue—that is, to the inhomogeneity of the tissue on

**TABLE 3. Overview of the Differences in Histology, Optical, and HR-MAS NMR Data Between SCF, ADF, NFAS, and IFAS**

| Measurement | IFAS versus NFAS, ADF, SCF | | | |
|---|---|---|---|---|
| Histology | Fat<br>↓ Fat concentration | Water<br>↑Cytoplasm (= water) | Collagen/Small cellular structures<br>↑Density of cell nuclei<br>↑Myelin<br>↑Collagen | Unknown |
| Absorption | ↓1200 and 1750 nm | ↑1300–1600<br>↑1900–2200 nm | ↑1300–1600 | Peak shift 900–1000 nm |
| DRS | ↓ Fat (%) | ↑ H2O (%) | ↑Scattering parameter (b) ↑Collagen concentration | |
| HR-NMR MAS | ↓ Lipid content | ↑ Water content | | Extra chemical peak shifts 3.0–3.2, 3.4, 5.7–5.8 ppm |

a sub wavelength scale. The high scattering parameter (b) observed by DRS in IFAS may therefore be related to inhomogeneity in the refractive index of IFAS tissue structures of a scale of 100–200 nm.

Other observations that are not easily explained include: the 1000-nm dip present most prominently in the DRS spectra of IFAS occurs at the same wavelength as the shifted optical absorption curve. This could be an OH overtone; the fact that this shift is observed in IFAS could be consistent with the higher water content in that tissue. However, the shift may be attributed to some other substance, like special myelin proteins only found in IFAS tissue [64,65]. The increased optical absorption between 1600 and 2300 nm is also not clearly explained but may be related to a CH combination band [66]. Also, the additional peaks observed in HR-NMR could not be directly related to the other measurements.

No significant inconsistencies between the findings from the different methods were observed.

Additional studies were performed to find an explanation for the additional peaks in the HR-NMR measurements. We suspected sphingomyelin to be the cause of these additional peaks, because it is a lipid found mainly in cell membranes of peripheral nerves, especially in the membranous myelin sheath that surrounds nerve cell [65,67]. Additionally, the myelin sheath of a peripheral nerve consists of typical proteins, like $P_0$ (>50% of the proteins), $P_1$, protein- 22, and 40% of water [65].

HR-MAS NMR was performed on pure cholesterol and sphingomyelin from chicken egg yolk (Sigma–Aldrich, Product Number S0756, white powder, >95% purity). Optical absorption and DRS measurements were performed in the sphingomyelin material. However, the results of those measurements failed to explain the additional HR-MAS NMR peaks in IFAS: the extra peaks in the HR-MAS NMR spectra do not match with the spectrum of pure cholesterol or sphingomyelin. Also, the DRS and absorption measurements of sphingomyelin did not show the same shifts and peaks as IFAS.

The extra search for molecular identification of the extra peak shifts by 2D $^{13}C$-$^{1}H$ HSQC confirmed the triglyceride lipid composition from HR-MAS NMR but failed to clearly explain the extra peaks of the unidentified compound (Supplements S1 and S2).

One possible explanation why we were not able to finally clarify the role of sphingomyelin is that sphingomyelin is strongly bound to the protein matrix inside nerve tissue and is therefore difficult to extract and dissolve [65]. We further note that *ex vivo* human protein-bound sphingomyelin and the sphingomyelin of chicken yolk are molecularly different; so, the used material might not have been the best to test the hypothesis. However, no alternative materials were readily available.

Comparing these results with the results of Hendriks et al. and Langhout et al., the differences in collagen, water, scattering, and fat were similar. This study did not find differences in β-carotene [32,46]. This may be due to individual differences between the cadavers, such as diet and percentage of subcutaneous fat, which influences β-carotene percentage.

This study expanded the optical database of the DRS of different human tissues. Optical data of blood, muscle, and fat are already well described [36–41,53,59]. The former *in vivo* studies used a spectrum from 500 to 1600 nm. This study demonstrates that it could be interesting to use a wider range to discriminate IFAS. A study performed by Schols et al. used DRS up to 1830 nm in an *in vivo* setting to differentiate adipose from nerve tissue [68]. Stelzle et al. reported optical nerve detection by DRS in pigs (*ex vivo*). They could differentiate between nerve tissue derived from bone and from salivary glands with a sensitivity of approximately 83% and a specificity of 78%. They used wavelengths ranging from 350 to 650 nm. Stelzle et al. did not focus on the differentiation of nerve tissue and adipose tissue [69].

There are some limitations to the work presented here that should be noted. First, the sample size is very limited. The results shown above focus on qualitative differences between the tissue types and the various methods to assess the biological, morphological, chemical and optical differences. For a quantitative assessment of the differences between the tissues and the correlation of DRS and HR-MAS-NMR or histology, many more samples are required.

Second, for the absorption spectrophotometry measurements, the Kubelka-Munk method was used to extract the absorption spectra from the measured transmittance and reflectance. For these measurements, it was challenging to keep the tissue homogeneous throughout the length of the measurement cuvette. This inhomogeneity likely explains some of the variability seen in the data. The exact same tissue could not be compared for all cadavers and all measurement types. Up to now, it is unclear what effects freezing, thawing, and re-freezing the tissue had on the DRS and optical absorption measurements. Additionally, the absorption coefficients can be calculated with alternative methods [52,54], such as inverse Monte Carlo or inverse adding-doubling, which are considered more accurate but also have their own limitations, like *a priori* knowledge of the absorbers present in the tissue samples or integrating sphere parameters. For the qualitative analysis presented here, we believe that the choice of method has not influenced our conclusions. For future, quantitative, assessments, more robust methods should be utilized.

Third, related to the DRS measurements, we note that the exact values of the chromophore concentrations obtained using the Farrell method are probably overestimated [48]. This is caused by the short distance between the source and detection fibers present in the needles; due to the short distance, the diffusion approximation used by the Farrell model is most likely not strictly valid. We have investigated the effect of the short distances by comparing results obtained with the diffusion approximation fitting with Monte Carlo calculations [70]. From those investigations, we have found that fit results using the diffusion approximation result in

overestimation of the chromophore concentrations. We believe that this limitation does not impact the conclusions of this study, since we are investigating and comparing trends in the data between the different tissue types. Additionally, the percentages of fat and water between the DRS and HR-MAS-NMR measurements result in very similar percentages. DRS also has limitations with respect to its chemical specificity. Another spectroscopic technique such as Raman spectroscopy has a much higher molecular specificity, however, at the cost of lower signal levels. The combination of Raman spectroscopy and HR-MAS-NMR as used to study vibrational assignments in food, agriculture and chemistry could possibly yield more insights when applied to IFAS [71,72].

## CONCLUSIONS

Histology, DRS spectra, light absorption, and HR-MAS NMR spectroscopy showed clear differences between fascicular nerve tissue and adipose tissues in an *ex vivo* human setting (Table 3). Collagen, water, fat, and cellular nuclei concentration might explain the majority of differences between nerve fascicular tissue and the other tissues. However, there may be other morphological, biological, or chemical differences that can also be used to differentiate fascicular tissue. The extra peaks observed in the absorption spectra and the HR-MAS NMR spectra of the IFAS samples may be additional differentiators; unfortunately though, we have not been able to identify the nature of these differences and further investigation in future studies is necessary. Honing in on these known and unknown differences can potentially improve the discriminatory capabilities of DRS incorporated in an anesthesiology needle, thereby changing clinical practice by giving live feedback during the procedure of the tissue characteristics in front of the needle.

## AVAILABILITY OF DATA AND MATERIALS

The datasets supporting the conclusions of this article are included within the article as supplement files 1 to 4.

## AUTHORS' CONTRIBUTIONS

A.J.R.B, T.B, H.v.I., M.v.K, A.L., and P.v.D. contributed to the study design, the clinical experiments, and the data analysis and wrote the manuscript. G.W.L. M.v.d.V., and B.H. initiated and contributed to the study design, the clinical experiments, the data analysis, and manuscript preparation.

## ACKNOWLEDGMENTS

The authors acknowledge Greet Mommen (www.greetmommen.be) for making the anatomical illustration and preparing the histological figures and Danielle Beelen for doing the HR-NMR measurements. Funding: Philips Research, Eindhoven, The Netherlands

## REFERENCES

1. Ilfeld BM, Morey TE, Wright TW, Chidgey LK, Enneking FK. Continuous interscalene brachial plexus block for postoperative pain control at home: A randomized, double-blinded, placebo-controlled study. Anesth Analg 2003;96:1089–1095, table of contents.
2. Abdallah FW, Macfarlane AJ, Brull R. The requisites of needle-to-Nerve proximity for ultrasound-Guided regional anesthesia: A scoping review of the evidence. Reg Anesth Pain Med 2016 41:221–228.
3. Sites BD, Brull R, Chan VW, et al. Artifacts and pitfall errors associated with ultrasound-guided regional anesthesia: Part II: A pictorial approach to understanding and avoidance. Reg Anesth Pain Med 2010;35:S81–S92.
4. Gadsden J, McCally C, Hadzic A. Monitoring during peripheral nerve blockade. Curr Opin Anaesthesiol 2010;23:656–661.
5. Hong JH, Huh B, Shin HH. Comparison between digital subtraction angiography and real-time fluoroscopy to detect intravascular injection during lumbar transforaminal epidural injections. Reg Anesth Pain Med 2014;39:329–332.
6. Lee MH, Yang KS, Kim YH, Jung HD, Lim SJ, Moon DE. Accuracy of live fluoroscopy to detect intravascular injection during lumbar transforaminal epidural injections. Korean J Pain 2010;23:18–23.
7. Chien GC, Candido KD. Digital subtraction angiography is not the answer for safe epidural injections. Pain Physician 2014;17:E413–E414.
8. O'Neil JMD. Musculoskeletal Ultrasound, Anatomy and Technique. New York: Spinger-Verlag New York; 2008. p 348.
9. Gray AT. Ultrasound-guided regional anesthesia: Current state of the art. Anesthesiology 2006;104:368–373, discussion 365A.
10. Perlas A, Niazi A, McCartney C, Chan V, Xu D, Abbas S. The sensitivity of motor response to nerve stimulation and paresthesia for nerve localization as evaluated by ultrasound. Reg Anesth Pain Med 2006;31:445–450.
11. Neal JM. Ultrasound-guided regional anesthesia and patient safety: An evidence-based analysis. Reg Anesth Pain Med 2010;35:S59–S67.
12. Terkawi AS, Karakitsos D, Elbarbary M, Blaivas M, Durieux ME. Ultrasound for the anesthesiologists: Present and future. ScientificWorldJournal 2013;2013:683685.
13. Neuburger M, Schwemmer U, Volk T, Gogarten W, Kessler P, Steinfeldt T. [Localization of peripheral nerves. Success and safety with electrical nerve stimulation]. Anaesthesist 2014;63:422–428.
14. Barrington MJ, Watts SA, Gledhill SR, et al. Preliminary results of the Australasian Regional Anaesthesia Collaboration: A prospective audit of more than 7000 peripheral nerve and plexus blocks for neurologic and other complications. Reg Anesth Pain Med 2009;34:534–541.
15. Jacob AK, Mantilla CB, Sviggum HP, Schroeder DR, Pagnano MW, Hebl JR. Perioperative nerve injury after total knee arthroplasty: Regional anesthesia risk during a 20-year cohort study. Anesthesiology 2011;114:311–317.
16. Auroy Y, Benhamou D, Bargues L, et al. Major complications of regional anesthesia in France: The SOS regional anesthesia hotline service. Anesthesiology 2002;97:1274–1280.
17. Orebaugh SL, Kentor ML, Williams BA. Adverse outcomes associated with nerve stimulator-guided and ultrasound-guided peripheral nerve blocks by supervised trainees: Update of a single-site database. Reg Anesth Pain Med 2012;37:577–582.
18. Barrington MJ, Snyder GL. Neurologic complications of regional anesthesia. Curr Opin Anaesthesiol 2011;24:554–560.
19. Houten JK, Errico TJ. Paraplegia after lumbosacral nerve root block: Report of three cases. Spine J 2002;2:70–75.
20. Helen L, O'Donnell BD, Moore E. Nerve localization techniques for peripheral nerve block and possible future directions. Acta Anaesthesiol Scand 2015;59:962–974.
21. Malhotra G, Abbasi A, Rhee M. Complications of transforaminal cervical epidural steroid injections. Spine (PhilaPa 1976) 2009;34:731–739.
22. Candido KD, Knezevic N. Cervical epidural steroid injections for the treatment of cervical spinal (neck) pain. Curr Pain Headache Rep 2013;17:314.
23. Helm S, Glaser S, Falco F, Henry B. A medical-legal review regarding the standard of care for epidural injections, with

particular reference to a closed case. Pain Physician 2010;13: 145–150.
24. Murthy NS, Maus TP, Behrns CL. Intraforaminal location of the great anterior radiculomedullary artery (artery of Adamkiewicz): A retrospective review. Pain Med 2010;11: 1756–1764.
25. Huntoon MA, Martin DP. Paralysis after transforaminal epidural injection and previous spinal surgery. Reg Anesth Pain Med 2004;29:494–495.
26. Kennedy DJ, Dreyfuss P, Aprill CN, Bogduk N. Paraplegia following image-guided transforaminal lumbar spine epidural steroid injection: Two case reports. Pain Med 2009;10: 1389–1394.
27. Auroy Y, Narchi P, Messiah A, Litt L, Rouvier B, Samii K. Serious complications related to regional anesthesia: Results of a prospective survey in France. Anesthesiology 1997;87: 479–486.
28. Moayeri N, Bigeleisen PE, Groen GJ. Quantitative architecture of the brachial plexus and surrounding compartments, and their possible significance for plexus blocks. Anesthesiology 2008;108:299–304.
29. Moayeri N, Groen GJ. Differences in quantitative architecture of sciatic nerve may explain differences in potential vulnerability to nerve injury, onset time, and minimum effective anesthetic volume. Anesthesiology 2009;111: 1128–1134.
30. Sala-Blanch X, Ribalta T, Rivas E, et al. Structural injury to the human sciatic nerve after intraneural needle insertion. Reg Anesth Pain Med 2009;34:201–205.
31. Bonnel F. Microscopic anatomy of the adult human brachial plexus: An anatomical and histological basis for microsurgery. Microsurgery 1984;5:107–118.
32. Hendriks BH, Balthasar AJ, Lucassen GW, et al. Nerve detection with optical spectroscopy for regional anesthesia procedures. J Transl Med 2015;13:380.
33. Steinfeldt T, Graf J, Schneider J, et al. Histological consequences of needle-nerve contact following nerve stimulation in a pig model. Anesthesiol Res Pract 2011;2011: 591851.
34. Bashkatov AN, Genina EA, Kochubey VI, Tuchin VV. Optical properties of the subcutaneous adipose tissue in the spectral range 400–2500 nm. Opt Spectrosc 2005;99:836–842.
35. Bashkatov AN, Genina EA, et al. Optical properties of human skin, subcutaneous and muscous tissues in the wavelength range from 400 t2000 nm. J Phys D 2005;38:2543–2555.
36. Rathmell JP, Desjardins AE, van der Voort M, et al. Identification of the epidural space with optical spectroscopy: An *in vivo* swine study. Anesthesiology 2010;113: 1406–1418.
37. Brynolf M, Sommer M, Desjardins AE, et al. Optical detection of the brachial plexus for peripheral nerve blocks: An *in vivo* swine study. Reg Anesth Pain Med 2011;36:350–357.
38. Desjardins AE, Hendriks BH, van der Voort M, et al. Epidural needle with embedded optical fibers for spectroscopic differentiation of tissue: *Ex vivo* feasibility study. Biomed Opt Express 2011;2:1452–1461.
39. Desjardins AE, van der Voort M, Roggeveen S, et al. Needle stylet with integrated optical fibers for spectroscopic contrast during peripheral nerve blocks. J Biomed Opt 2011;16: 077004.
40. Balthasar A, Desjardins AE, van der Voort M, et al. Optical detection of vascular penetration during nerve blocks: An *in vivo* human study. Reg Anesth Pain Med 2012;37:3–7.
41. Balthasar A, Desjardins AE, van der Voort M, et al. Optical detection of peripheral nerves: An *in vivo* human study. Reg Anesth Pain Med 2012;37:277–282.
42. Schenkman KA, Marble DR, Feigl EO, Burns DH. Near infrared spectroscopic measurement of myoglobin oxygen saturation in the presence of hemboglobin using partial least-squares analysis. Appl Spectrosc 1999;53:325–331.
43. Kondepati VR, Heise HM, Backhaus J. Recent applications of near-infrared spectroscopy in cancer diagnosis and therapy. Anal Bioanal Chem 2008;390:125–139.
44. Bydlon TM, Nachabe R, Ramanujam N, Sterenborg HJ, Hendriks BH. Chromophore based analyses of steady-state diffuse reflectance spectroscopy: Current status and perspectives for clinical adoption. J Biophotonics 2015;8:9–24.
45. Balthasar AJ, Lucassen GW, Sommer M, et al. The role of spectral tissue sensing during lumbar transforaminal epidural injection. Reg Anesth Pain Med 2016;41:520–526.
46. Langhout GC, Kuhlmann KFD, Wouters M, et al. Nerve detection during surgery: Optical spectroscopy for peripheral nerve localization. Lasers Med Sci 2018;33:619–625.
47. Langhout GC, Bydlon TM, van der Voort M, et al. Nerve detection using optical spectroscopy, an evaluation in four different models: In human and swine, *in-vivo*, and *post mortem*. Lasers Surg Med 2018;50:253–261.
48. Farrell TJ, Patterson MS, Wilson B. A diffusion theory model of spatially resolved, steady-state diffuse reflectance for the noninvasive determination of tissue optical properties *in vivo*. Med Phys 1992;19:879–888.
49. Kiernan J. Histological and Histochemical Methods: Theory and Practice. UK: Scion; 2008.
50. Di Scipio F, Raimondo S, Tos P, Geuna S. A simple protocol for paraffin-embedded myelin sheath staining with osmium tetroxide for light microscope observation. Microsc Res Tech 2008;71:497–502.
51. Romeis—Mikroskopische Technik. Springer Berlin Heidelberg, 2015.
52. Tuchin V. Tissue optics—Light scattering methods and instruments for medical diagnosis. Bellingham: SPIE; 2007.
53. Nachabe R, Hendriks BH, Desjardins AE, van der Voort M, van der Mark MB, Sterenborg HJ. Estimation of lipid and water concentrations in scattering media with diffuse optical spectroscopy from 900 to 1,600nm. J Biomed Opt 2010;15:037015.
54. Bargo PR, Prahl SA, Goodell TT, et al. *In vivo* determination of optical properties of normal and tumor tissue with white light reflectance and an empirical light transport model during endoscopy. J Biomed Opt 2005;10:034018.
55. Zonios G, Bassukas I, Dimou A. Comparative evaluation of two simple diffuse reflectance models for biological tissue applications. Appl Opt 2008;47:4965–4973.
56. Sun J, Fu K, Wang A, Lin AW, Utzinger U, Drezek R. Influence of fiber optic probe geometry on the applicability of inverse models of tissue reflectance spectroscopy: Computational models and experimental measurements. Appl Opt 2006;45:8152–8162.
57. Reif R, A'Amar O, Bigio IJ. Analytical model of light reflectance for extraction of the optical properties in small volumes of turbid media. Appl Opt 2007;46:7317–7328.
58. Amelink A, Sterenborg HJ, Bard MP, Burgers SA. *In vivo* measurement of the local optical properties of tissue by use of differential path-length spectroscopy. Opt Lett 2004;29: 1087–1089.
59. Nachabe R, Hendriks BH, van der Voort M, Desjardins AE, Sterenborg HJ. Estimation of biological chromophores using diffuse optical spectroscopy: Benefit of extending the UV-VIS wavelength range to include1000 to 1600 nm. Biomed Opt Express 2010;1:1432–1442.
60. Nachabe R, Evers DJ, Hendriks BH, et al. Diagnosis of breast cancer using diffuse optical spectroscopy from 500 to1600 nm: Comparison of classification methods. J Biomed Opt 2011;16: 087010.
61. Bigeleisen PE. Nerve puncture and apparent intraneural injection during ultrasound-guided axillary block does not invariably result in neurologic injury. Anesthesiology 2006;105:779–783.
62. Sermeus L, Sala-Blanch X. Ultrasound-guided block and the incidence of intraneural injection. A reply. Anaesthesia 2017;72:914–915.
63. Hara K, Sakura S, Yokokawa N, Tadenuma S. Incidence and effects of unintentional intraneural injection during ultrasound-guided subgluteal sciatic nerve block. Reg Anesth Pain Med 2012;37:289–293.
64. Paszek M, Weaver V. Biophysics. Enforcing order on signaling. Science 2010;327:1335–1336.
65. Chapter 4. Myelin Formation SaB, Quarles. PMaRH. Chapter 4. Myelin Formation, Structure and Biochemistry Pierre Morell and Richard H Quarles. Lippincott-Raven: Philadelphia, 1999.
66. Stuart A, Fysh DAJS, Fredericks PM. Near-Infrared diffuse reflectance spectroscopy of coal. Appl Spectrosc 1985;29:354–357.

67. Ramstedt B, Slotte JP. Membrane properties of sphingomyelins. FEBS Lett 2002;531:33–37.
68. Schols RM, ter Laan M, Stassen LP, et al. Differentiation between nerve and adipose tissue using wide-band (350–1,830nm) *in vivo* diffuse reflectance spectroscopy. Lasers Surg Med 2014;46:538–545.
69. Stelzle F, Zam A, Adler W, et al. Optical nerve detection by diffuse reflectance spectroscopy for feedback controlled oral and maxillofacial laser surgery. J Transl Med 2011;9:20.
70. Zhu C, Liu Q. Review of Monte Carlo modeling of light transport in tissues. J Biomed Opt 2013;18:50902.
71. Kose E, Bardak F, Atac A, Karabacak M, Cipiloglu MA. Determination of structural and vibrational spectroscopic features of neutral and anion forms of dinicotinic acid by using NMR, infrared and Raman experimental methods combined with DFT and HF. Spectrochim Acta A Mol Biomol Spectrosc 2013;114:38–45.
72. Chong CK, Xing J, Phillips DL, Corke H. Development of NMR and raman spectroscopic methods for the determination of the degree of substitution of maleate in modified starches. J Agric Food Chem 2001;49:2702–2708.

## SUPPORTING INFORMATION

Additional supporting information may be found online in the Supporting Information section at the end of the article.